

Monitoring Early Changes in Tumor Metabolism in Response to Therapy Using Hyperpolarized ¹³C MRSI in a Preclinical Model of Glioma

Heeseung Lim¹, Francisco Martínez-Santesteban¹, Michael D. Jensen¹, Albert Chen², Eugene Wong^{1,3,4}, and Timothy J. Scholl^{1,5,6}

¹Department of Medical Biophysics, Western University, London, ON, Canada; ²General Electric Healthcare, Toronto, ON, Canada; Departments of ³Physics and Astronomy; ⁴Oncology; and ⁵Robarts Research Institute, Western University, London, ON, Canada, and ⁶Ontario Institute for Cancer Research, Toronto, ON, Canada

Corresponding Author:

Timothy J. Scholl, PhD

1151 Richmond St. N., London, Ontario, Canada N6A 5B7;

E-mail: scholl@uwo.ca

Key Words: Hyperpolarized ¹³C, pyruvate, tumor metabolism, therapeutic response, glioma

Abbreviations: 2-deoxy-2-[18F]fluoro-D-glucose (18F-FDG), analysis of variance (ANOVA), field of view (FOV), hematoxylin & eosin (H&E), lactate-to-pyruvate ratio (Lac/Pyr ratio), lactate dehydrogenase (LDH), magnetic resonance imaging (MRI), magnetic resonance spectroscopic imaging (MRSI), positron emission tomography (PET), Response Assessment in Neuro-Oncology (RANO), Response Evaluation Criteria in Solid Tumors (RECIST), echo time (TE), repetition time (TR)

ABSTRACT

This study shows the use of hyperpolarized ¹³C magnetic resonance spectroscopic imaging (MRSI) to assess therapeutic efficacy in a preclinical tumor model. ¹³C-labeled pyruvate was used to monitor early changes in tumor metabolism based on the Warburg effect. High-grade malignant tumors exhibit increased glycolytic activity and lactate production to promote proliferation. A rodent glioma model was used to explore altered lactate production after therapy as an early imaging biomarker for therapeutic response. Rodents were surgically implanted with C6 glioma cells and separated into 4 groups, namely, no therapy, radiotherapy, chemotherapy and combined therapy. Animals were imaged serially at 6 different time points with magnetic resonance imaging at 3 T using hyperpolarized [1-¹³C]pyruvate MRSI and conventional ¹H imaging. Using hyperpolarized [1-¹³C]pyruvate MRSI, alterations in tumor metabolism were detected as changes in the conversion of lactate to pyruvate (measured as Lac/Pyr ratio) and compared with the conventional method of detecting therapeutic response using the Response Evaluation Criteria in Solid Tumors. Moreover, each therapy group expressed different characteristic changes in tumor metabolism. The group that received no therapy showed a gradual increase of Lac/Pyr ratio within the tumor. The radiotherapy group showed large variations in tumor Lac/Pyr ratio. The chemo- and combined-therapy groups showed a statistically significant reduction in tumor Lac/Pyr ratio; however, only combined therapy was capable of suppressing tumor growth, which resulted in low endpoint mortality rate. Hyperpolarized ¹³C MRSI detected a prompt reduction in Lac/Pyr ratio as early as 2 days post combined chemo- and radiotherapies.

INTRODUCTION

Brain cancer is a challenging disease with very poor prognosis and outcomes. The most prevalent form of malignant brain tumors is glioma, which arises from glial cells (1). Although there are aggressive therapies available (ie, surgical resection, radiotherapy, and chemotherapy), patients diagnosed with the most aggressive (grade IV) malignant glioma have a disappointing 5-year survival rate of 5.1% (2). Despite aggressive treatment, these tumors almost inevitably recur (3).

Advances in imaging techniques help radiologists to noninvasively detect and assess brain tumors. Magnetic resonance imaging (MRI) is the preferred clinical diagnostic tool for brain

tumor detection (4); yet, it remains challenging to observe both the therapeutic response and efficacy during the course of the treatments. Because radiotherapy and chemotherapy affect tumors at the molecular level (DNA damage, blocking protein/RNA), phenotypical changes (tumor size, diffusion, proliferation) that arise from therapies, can be challenging to detect during the early stages of treatment.

Clinical assessment of the progression of a primary brain tumor can be assessed by contrast-enhanced MRI using one of the following criteria: Response Assessment in Neuro-Oncology (RANO) criteria, Response Evaluation Criteria in Solid Tumors (RECIST), or World Health Organization criteria (5, 6). The RANO

criteria, updated from MacDonald criteria, includes measurable morphological changes in the tumor size due to therapy. Tumor response is divided into 4 different groups based on changes in contrast-enhancing tumor volumes:

1. complete response with no tumor enhancement;
2. partial response with >50% reduction in tumor size;
3. progressive disease with >25% increase in tumor size; and
4. stable disease with no changes in tumor size.

Other criteria methods use similar categorizations of groups but differ in methodology for measurement of tumor size. All criteria methods depend on the post contrast-enhancement of tumors visualized using MRI. However, it is often difficult to determine if the enhancement is a result of tumor reoccurrence, radiation necrosis, or pseudoprogression (5).

Tumor metabolism has been identified as a hallmark of cancer (7). Tumors require an increased amount of energy and nutrients to proliferate at a much faster rate compared with healthy tissues. To sustain increased energy demands, tumor metabolism is altered (8). Most notably, energy production in tumor cells often switches from predominantly oxidative phosphorylation in the mitochondria (Krebs cycle) to anaerobic glycolysis (followed by lactic acid fermentation) in the cytosol even under the presence of oxygen (also known as Warburg effect) (9, 10). This choice of energy production generates an intracellular pool of lactic acid as a potential molecular imaging biomarker (11). Moreover, the excretion of lactic acid and protons from tumor cells accelerates acidification of the extracellular space and increases the viability of these cells through further vascularization (10). Clinical studies have shown an increased metabolic uptake of 2-deoxy-2- ^{18}F fluoro-(D)-glucose (^{18}F -FDG) in tumors using positron emission tomography (PET) (12, 13). The ability to monitor therapeutic changes accurately and in a timely manner in brain tumors will provide a further understanding of tumor metabolism and guide initiation of alternative (or salvage) therapies.

Hyperpolarized ^{13}C magnetic resonance spectroscopic imaging (^{13}C MRSI) is an emerging molecular imaging tool with MRI that can directly quantify metabolic changes in tissues. A chosen cellular substrate is enriched with ^{13}C and then hyperpolarized (highly magnetized) in the polarizer to increase the potential ^{13}C MRSI signal by nearly 5 orders of magnitude (14). After injection of the hyperpolarized ^{13}C -enriched substrate, the substrate and its by-products from metabolic processes can be individually detected in vivo by their inherent chemical shifts using magnetic resonance. The hyperpolarized signal is transient as the magnetization of the ^{13}C nuclei relaxes to thermal equilibrium. This is highly dependent on the hyperpolarized contrast agent's spin-lattice relaxation time (T1) and that of its metabolic by-products (15).

The most common and widely researched hyperpolarized ^{13}C contrast agent is $[1-^{13}\text{C}]$ pyruvate (16). After a bolus injection and circulation, hyperpolarized $[1-^{13}\text{C}]$ pyruvate is taken up by cells through active transport (17) and converted into 3 major metabolites, namely, $[1-^{13}\text{C}]$ alanine, ^{13}C bicarbonate, and $[1-^{13}\text{C}]$ lactate (16). Tumors exhibit increased lactate production through upregulated lactate dehydrogenase (LDH) production by oncogenes (9). Cells targeted by metabolic therapy have reduced LDH activity and thereby often exhibit

reduced lactate production (18, 19). The production of $[1-^{13}\text{C}]$ lactate in tumor tissues by metabolizing injected hyperpolarized $[1-^{13}\text{C}]$ pyruvate can be tracked using ^{13}C MRSI. In this way, the therapeutic response of tumors is monitored by measuring changes in $[1-^{13}\text{C}]$ lactate conversion from $[1-^{13}\text{C}]$ pyruvate. The effects of upregulated LDH activity in tumors measured by hyperpolarized ^{13}C MRSI have been previously reported in the literature (20–22).

Both glioma and brain tissues are highly metabolic and readily uptake metabolites for energy. This reduces the contrast and effectiveness of ^{18}F -FDG PET for imaging and quantification of brain tumors that must be confirmed by other means (13, 23, 24). For instance, brain tissue expresses high background signal with ^{18}F -FDG PET, particularly in the cortex, owing to high metabolic activity (25). In contrast, pyruvate is actively taken up by glioma cells through monocarboxylate transport and are rapidly converted to lactate by upregulated LDH activity (26, 27). Glioma cells are highly proliferative, using the lactate as an alternative energy source and for amino acid production (11). Thus, MRSI of hyperpolarized $[1-^{13}\text{C}]$ pyruvate has an advantage of directly measuring metabolic activity in glioma cells and the ability to distinguish these cells from other highly metabolic brain tissues through their altered metabolic signature.

The purpose of this study was to monitor the metabolic response of tumors to chemo- and radiotherapies using hyperpolarized ^{13}C MRSI in an orthotopic rodent model of glioma and compare with conventional methods of treatment response assessment. In previous work using hyperpolarized $[1-^{13}\text{C}]$ pyruvate, the separate effects of radiotherapy (28) and chemotherapy (29, 30) on tumor growth have been individually studied and reported. This study compares the effect of these different therapies and their combined use on tumor progression in a controlled longitudinal study. Because each therapy relies on a different treatment mechanism, we might expect that this will produce different metabolic responses to treatment. As discussed above, tumor response to therapy can be assessed by the observed ratio of $[1-^{13}\text{C}]$ lactate with respect to $[1-^{13}\text{C}]$ pyruvate in the cytosol of tumor cells by use of ^{13}C MRSI. The results of this study illustrate the ability of ^{13}C MRSI of hyperpolarized $[1-^{13}\text{C}]$ pyruvate to quantify therapeutic response for different therapies and to follow tumor progression or response with noninvasive longitudinal imaging.

METHODOLOGY

Pyruvic Acid Sample Preparation

A trityl radical, OX63 (Oxford Instruments, Concord, MA) was mixed with 99%-enriched $[1-^{13}\text{C}]$ pyruvic acid (Sigma Aldrich, Miamisburg, OH) to a final concentration of 15mM. The pyruvic acid preparation was stirred and heated to 60°C to dissolve, and then cooled and stored at -4°C for later use. Before hyperpolarization, ProHance (Bracco Diagnostics, Monroe Township, NJ), a paramagnetic contrast agent, was added at a concentration of 1mM to the pyruvic acid sample to enhance polarization and reduce polarization time (31).

Hyperpolarization

A Hypersense dynamic nuclear polarizer (Oxford Instruments, Abingdon, UK) was used to hyperpolarize the prepared $[1-^{13}\text{C}]$

pyruvic acid sample. The dynamic nuclear polarization operates at a temperature of 1.4 K and a magnetic field strength of 3.35 T. The pyruvic acid preparation was irradiated with microwaves from a source operating at 94.125 GHz achieving ~90% nuclear polarization of the solid after 45 minutes. For dissolution, the sample was rapidly thawed and mixed with a superheated 80mM phosphate buffer solution containing 0.34-mmol/L ethylenediaminetetraacetic acid. The resulting solution was dispensed into a flask prior to uptake into a syringe for injection. The resulting 80mM hyperpolarized [1-¹³C] pyruvate buffered solution had a final volume of ~4 mL with a pH of 7.4 at 37°C. The measured T1 for the ¹³C nucleus was ~65 seconds at 3 T (15) and its polarization was >12% in the liquid state.

In Vivo Imaging

All imaging sessions were performed using a GE Discovery MR750 3.0 T MRI (General Electric Healthcare, Waukesha, WI). A custom-built, switch-tuned ¹³C-¹H radiofrequency coil with a local ¹³C receive-only radiofrequency coil was used in transmit-only/receive-only operating mode for ¹³C imaging (32). Switch-tuning between ¹H and ¹³C frequencies produced inherently registered images for morphology (¹H) and metabolism (¹³C). A single imaging session consisted of (in sequential order) T2-weighted ¹H imaging, hyperpolarized ¹³C MRSI, dynamic susceptibility contrast imaging and post-Gd contrast T1-weighted ¹H imaging. T2-weighted ¹H images were acquired using a fast spin echo pulse sequence with the following imaging parameters: 80- × 80-mm field of view (FOV), 0.3-mm isotropic in-plane resolution, 3-mm slice thickness, repetition time (TR) = 4000 milliseconds, echo time (TE) = 85 milliseconds, bandwidth = 10.42 Hz, echo train length = 16, and number of averages = 4. For hyperpolarized ¹³C MRSI, animals were injected in the tail vein with ~3 mL of bolus of the buffered hyperpolarized [1-¹³C]pyruvate solution over a timed 12-second interval. Two-dimensional ¹³C-spectral maps were acquired 25 seconds after the injection using free induction decay chemical shift imaging with the following parameters: 60- × 60-mm FOV, 5-mm isotropic in-plane resolution, slice thickness = 10 to 15 mm (depending on tumor extent), flip angle = 10°, TR = 80 milliseconds, spectral width = 5000 Hz, and number of points = 256. Regional ¹³C-spectra are shown in Figure 1. Before T1-weighted ¹H imaging, 100mM of Magnevist (Bayer HealthCare Pharmaceuticals Inc., Whippany, NJ) was injected by a tail vein catheter. T1-weighted ¹H images were acquired using a fast gradient echo pulse sequence with the following parameters: 80- × 40- × 32-mm FOV, 0.5-mm isotropic resolution, flip angle = 25°, TR = 6.9 milliseconds, TE = 2.9 milliseconds, and 9 averages.

Animal Disease Model

Eighteen male Wistar rats (Charles River Laboratories, Senneville, QC, Canada) with an initial weight of ~250 g (~5- to 7-week old) were used for this study. One million rat glioma cells C6 (CCL-107, Purchased 2011, American Type Culture Collection, Manassas, VA) were stereotactically implanted in the caudate nucleus of the right brain hemisphere (day 0). C6 cells were passaged 9 times and tested for mycoplasma using MycoAlert™ (Lonza, Mississauga, ON, Canada) before use. Seven days post cell implantation, animals underwent pretherapy imaging sessions. On day 10, animals were randomly divided into the following 4 groups:

1. no therapy;
2. radiotherapy;
3. chemotherapy; and
4. combined radio- and chemotherapy.

Group 1 (no therapy) functioned as the control group. The radiotherapy group received a tumor-localized radiation dose of 20 Gy in 2 fractions on 2 consecutive days to the tumor using a modified μ CT GE Vision 120CT (General Electric Healthcare, Waukesha WI) with a custom-built collimator (33). The chemotherapy group received intraperitoneal injections of 40 mg/kg of temozolomide (Sigma Aldrich, Miamisburg, OH) dissolved in dimethyl sulfoxide for 5 consecutive days. The combined therapy group received both therapies, with the same timeline as described above. Starting on day 12, and every 3 days thereafter, animals underwent post-therapy imaging sessions. At endpoint, rats were sacrificed for histological examination. All animal procedures were approved by the University Council on Animal Care, Animal Use Subcommittee.

Histology

Following the final post-therapy imaging session, the rats were injected by a tail vein catheter with 60-mg/kg pimonidazole (Hypoxyprobe Inc., Burlington, MA) 30 minutes before sacrifice. The rats were then sacrificed, perfused with 4% paraformaldehyde (Sigma Aldrich, Miamisburg, OH), and the brains were extracted and refrigerated at 5°C in 4% paraformaldehyde. The brains were then sectioned to 5-mm-thick paraffin slabs and later further sectioned to 5 μ m for staining. Brain sections were stained with hematoxylin & eosin (H&E) and for hypoxia. Whole-brain sectioned slices were scanned using light-fluorescent microscopy (Leica Microsystems Inc., Concord, ON, Canada). Histological image slices were coregistered to the MRI images using Slicer (Version 4.31, Surgical Planning Laboratory, Brigham & Women's Hospital, Boston, MA) using a custom software plugin (34).

Image Analysis

The ¹³C MRSI raw data were analyzed using a custom-written MATLAB (MathWorks, Natick, MA) script. Free induction decay signals from each *k*-space point were apodized by a 20-Hz Gaussian filter. The signals were spatially zero-filled and then Fourier-transformed in frequency and phase-encoding directions. Signal for an individual metabolite is represented by the time-domain signal function as described in a study (35):

$$S(t) = Ae^{-i\Omega t + \phi} e^{-R_2^* t}. \quad (1)$$

Here, $S(t)$ is the signal at time t , A is the amplitude of the signal, Ω is the frequency offset, and ϕ is the phase offset. R_2^* is the effective spin-spin relaxation rate given by $R_2^* = \frac{1}{T_2}$. Each voxel could potentially contain up to 5 different summed metabolite signals. Initial estimates for the parameters for each individual metabolite (A_i , Ω_i , ϕ_i , and $R_{2,i}^*$) were obtained by examining the data. The summed signal model for all observed metabolites was fitted to the processed data by a nonlinear least-squares curve-fitting method on a voxel-by-voxel basis to extract metabolite parameters and their uncertainties. Amplitudes of lactate and

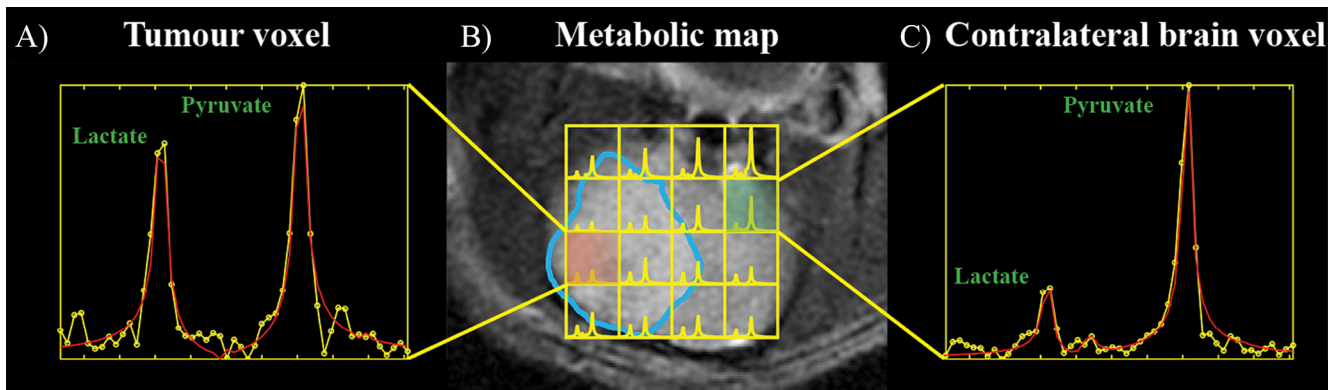


Figure 1. Hyperpolarized ^{13}C spectra of a rat brain with tumor. (A) and (C) Individual spectra from tumor and contralateral brain voxels. Regional spectral data overlaid on T2-weighted image (B). Tumor has been outlined in cyan. Red lines represent line fitting to spectral data in yellow. Note the increased lactate signal relative to pyruvate signal in the tumor voxel.

pyruvate were used to calculate the lactate-to-pyruvate ratio (Lac/Pyr ratio), and its fitting errors were used to propagate an associated uncertainty. An example of spectral fitting and maps are showing in Figure 1. Voxels containing $>50\%$ of tissue of interest were used for measurements.

Statistical Analysis

All statistics were analyzed using SPSS statistics software (IBM Corp., Armonk, NY). Post-Gd tumor volumes were measured from the T1-weighted contrast images using ITK-Snap [www.itksnap.org (36)]. Boundaries of tumors were manually contoured and the volumes were calculated. Interobserver variability was used to estimate tumor volume errors. Tumor growth rates were modeled from longitudinal measurements of tumor volume. Fitted amplitudes for the lactate and pyruvate signals were used to calculate the Lac/Pyr ratio, and the individual fitting errors were used to propagate an associated uncertainty for the ratio. Voxels that contains $<50\%$ of a specific tissue of interest were used for measurement. Tumor and contralateral brain tissues were identified using ^1H imaging data. A tumor was manually segmented and then a similar region and size of brain were segmented on the contralateral side. If the tumor had expanded to the other hemisphere, a contralateral brain segmentation from a previous experimental time point (excluding tumor) was used. The average Lac/Pyr ratio and its uncertainty for a specific group at a single time point were calculated from all identified voxels from all animals comprising the group for that specific time point. The correlations between the Lac/Pyr ratio, tumor volume, and tumor growth rate were tested using Pearson correlation. Analysis of variance (ANOVA) with Dunnett's post hoc test was performed to calculate the statistical differences between groups on each day and overall group differences, respectively. The uncertainties propagated from parameter fitting were used to weigh the Lac/Pyr ratios for ANOVA. Uncertainties for the Lac/Pyr ratio are reported as standard error of the mean of measurements.

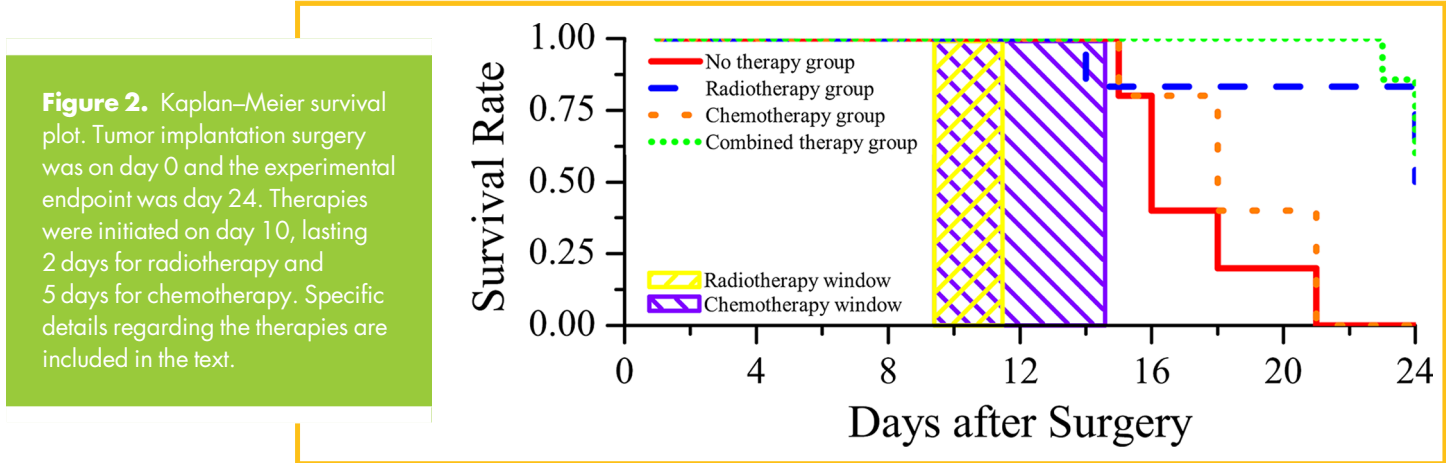
RESULTS

A total of 18 rodents were monitored using hyperpolarized $[1-^{13}\text{C}]$ pyruvate MRSI at multiple time points—7, 12, 15, 18, 21

and 24 days after tumor implantation. During the course of the longitudinal study, the health of some animals deteriorated owing to the increased tumor burden, and these animals were sacrificed earlier than the intended endpoint. Figure 2 depicts the survival rate of each group. The radiotherapy and combined therapy groups had the highest mean survival time at 25 days followed by the chemotherapy group at 18 d and lastly the no therapy group at 17 days. A Kaplan–Meier method was used to determine if there were any differences in the survival distribution for the therapy groups. The survival distributions for different therapy groups are statistically different ($P < .0005$).

Figures 3 and 4 illustrate longitudinal assessments of therapeutic response in a rat model of glioma comparing the Lac/Pyr ratio and tumor volume. Figure 3 shows longitudinal imaging data for a representative rodent from the no therapy group. Rapid tumor growth is readily apparent in Figure 3A and is quantified in 3C. Longitudinal measurements of the Lac/Pyr ratio are presented in Figure 3B, comparing tumor and contralateral brain for each ^{13}C imaging session. Higher Lac/Pyr ratios are observed in tumor tissue than in contralateral brain tissue. The Lac/Pyr ratio increases with tumor growth. As shown in Figure 3C, without any therapy, the tumor grew rapidly. Owing to the heavy tumor burden and the resulting adverse health effects; the rodent was sacrificed before the last imaging session at day 24, in compliance with terms of the animal use protocol. Neurological impairment and lack of appetite were observed for all rodents that did not receive therapy, and as a result, these animals were sacrificed before the final imaging time point, typically between days 15 and 21.

Figure 4 shows a representative rodent from the combined therapy group. Tumor growth shown in Figure 4A and quantified in 4C is slower than that of the no therapy group. On day 7, the Lac/Pyr ratio is higher in the tumor than in contralateral brain tissue (Figure 4B). Within 2 days post therapy, the tumor Lac/Pyr ratio drops to that of contralateral brain. Further longitudinal measurements show similar Lac/Pyr ratios in tumor and healthy brain until the final imaging session on day 24. Reduced tumor



growth assessed by volume measurements commensurate with therapeutic response was not apparent until day 21.

Figure 5 illustrates a longitudinal comparison of the average Lac/Pyr ratio in tumors for the 4 therapy groups measured up to 24 days post cell implantation. A consistently elevated Lac/Pyr ratio was observed in the tumors for the no therapy group for all time points. No statistical comparison between the no therapy and other treatment groups was possible for days 21 and 24 owing to the poor survival of the untreated group. Some of the rodents that received radiotherapy showed a Lac/Pyr ratio reduction in the tumor tissue at day 12, but as a whole, that group did not show a significant reduction ($P = .33$). The rodents that received either chemotherapy or combined therapy show a statistically significant reduction in the Lac/Pyr ratio within the tumor volumes ($P < .05$) post therapy (days 12, 15 and 18). However, the rodents that received only chemotherapy did not survive to the endpoint at day 24 despite a significant reduction in the

Lac/Pyr ratio. Owing to rapid tumor growth, untreated animals met humane criteria for early euthanasia as early as day 18. As a result, by days 21 and 24, there was an insufficient number of rodents in the no therapy group to test significance with other groups. Application of combined therapy produced the best therapeutic response as assessed by the tumor Lac/Pyr ratio and confirmed by the survival data.

Tumor volume measurement from T1-weighted post-Gd images (data not shown) shows similar trends as the Lac/Pyr ratio. In the absence of therapy, tumor volumes significantly increased in size until animals were sacrificed. The average enhancing tumor volume in the no therapy group at endpoint was $384 \pm 63 \text{ mm}^3$. All therapies showed reduced tumor growth by endpoint assessed by volume measurement. The average enhancing tumor volume for chemotherapy, radiotherapy, and combined therapies were 140 ± 23 , 107 ± 18 , and $54 \pm 9 \text{ mm}^3$, respectively, at endpoint. Rodents with tumors that received

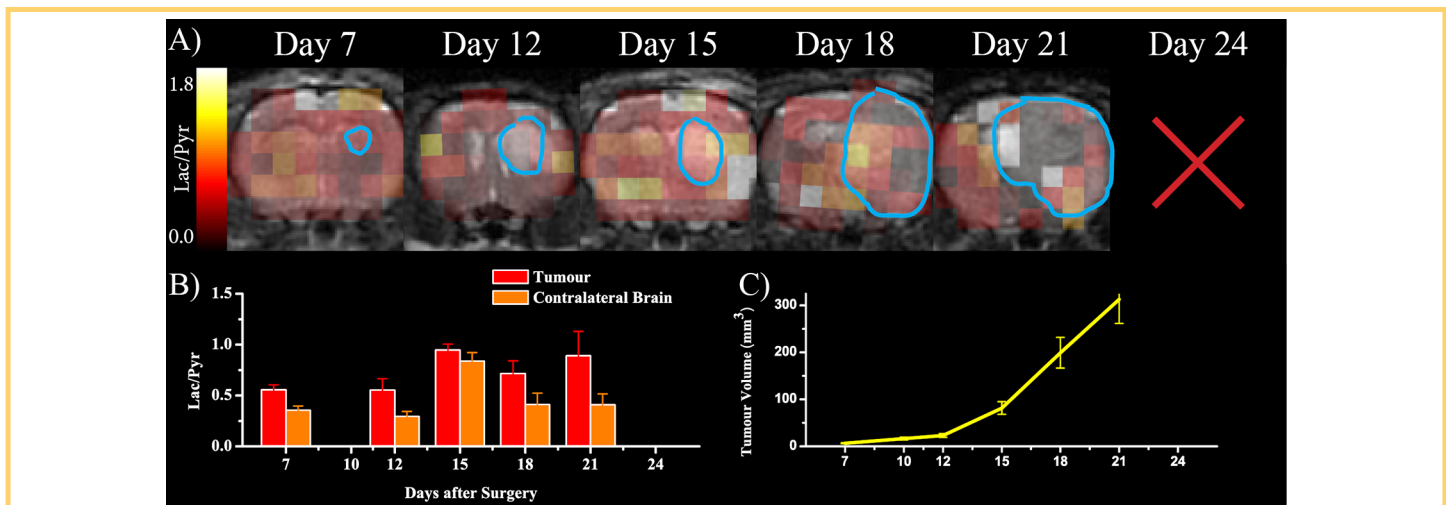


Figure 3. Representative animal from the *no therapy* group. Lactate-to-pyruvate ratio maps are overlaid on axial proton images of the rat brain at longitudinal imaging time points (A). Tumors are outlined by cyan boundaries. Bar graph of measured lactate-to-pyruvate ratio of tumors and contralateral brain volumes at different imaging sessions (B). Graph of tumor volumes (mm^3) at different imaging sections (C).

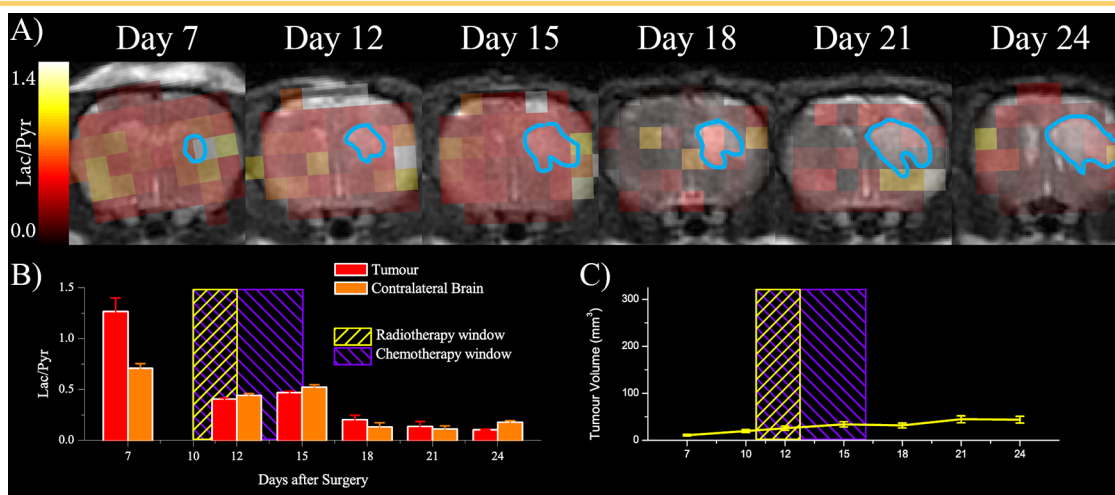


Figure 4. Representative animal from the *combined therapy* group. Lactate-to-pyruvate ratio maps are overlaid on axial proton images of the rat brain at longitudinal imaging time points (A). Tumors are outlined by cyan boundaries. Bar graph of measured lactate-to-pyruvate ratio of tumors and contralateral brain volumes at different imaging sessions (B). Graph of tumor volumes (mm³) at different imaging sections (C). Treatment periods are indicated as hatched areas.

radiotherapy and combined therapy would be classified as stable disease based on the RANO criteria. Whereas, for rodents with tumors that received chemotherapy, the observed tumor growth rate would produce a classification of progressive disease. Notably, when using only the T1-weighted post-Gd images as one would in the clinic, these classifications would be possible only as early as 18 days after cell implantation.

Furthermore, the correlations of tumor Lac/Pyruvate ratio versus tumor volume and growth rate are presented in Figure 6. The Pearson correlation coefficients for these data are 0.287 ($P = .105$) and 0.66 ($P < .001$) respectively. The tumor Lac/Pyruvate ratio was not correlated with tumor volume; however, a strong positive correlation with tumor growth rate was observed (Pearson correlation coefficient ~ 0.65).

Figure 6 presents the representative histological results comparing rodents that received either no therapy or combined therapy. The T2-weighted image, Lac/Pyruvate ratio images, and

histological sections have been coregistered as described in the Methods section. The tumors within the brain are easily distinguishable by ¹H MRI and H&E staining. The Lac/Pyruvate ratio and hypoxia staining show similar contrast between tumor and contralateral brain tissues. Comparing contralateral brain and tumor measurements, rodents that did not receive therapy showed higher Lac/Pyruvate ratio activity and hypoxia within the tumor, whereas animals that received combined therapy had minimal Lac/Pyruvate ratio activity through the entire brain and no hypoxia signal within the tumor at endpoint.

DISCUSSION

The goal of this study was to show the ability to detect early changes in therapeutic response in tumors using hyperpolarized [¹⁻¹³C]pyruvate MRSI and to evaluate potential clinical translation. Targeted therapy of tumor metabolism has gained more

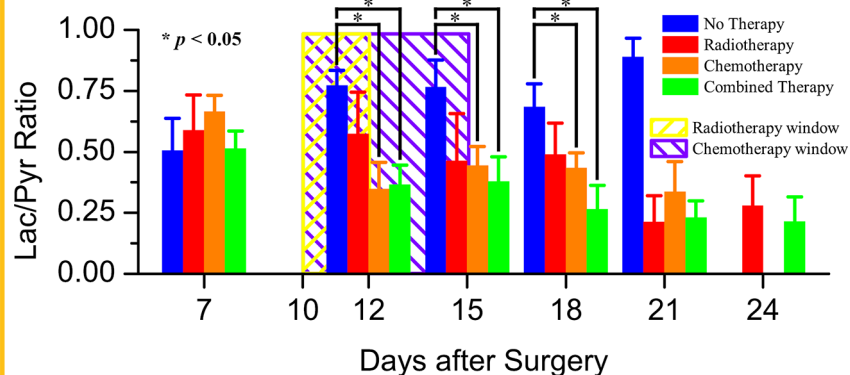


Figure 5. Longitudinal assessment of the lactate-to-pyruvate ratio in tumor tissue for 4 therapy groups. Radio- and chemotherapy were initiated on day 10 for a duration of 2 and 5 days, respectively. No statistical comparison between the no therapy and other therapy groups was possible for days 21 and 24 owing to the poor survival of the untreated group. (Details of therapy are in the text.)

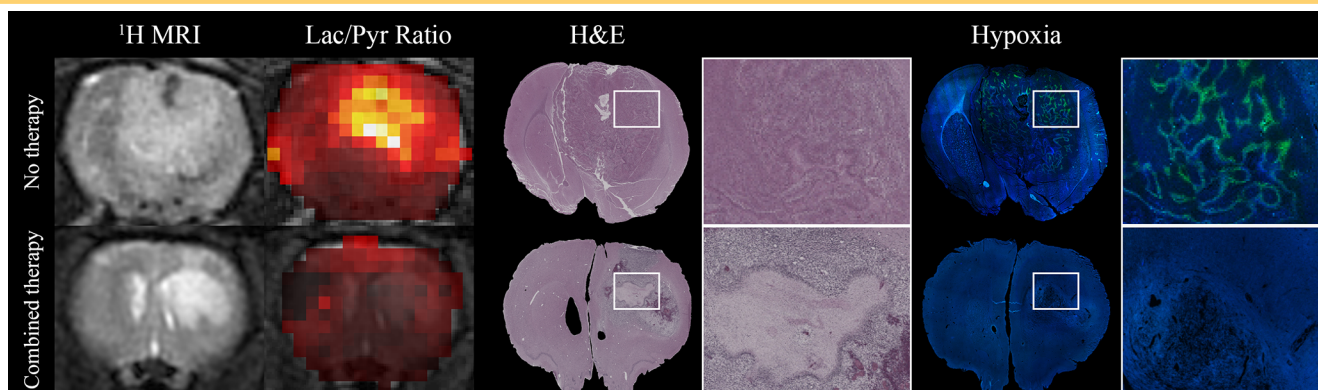


Figure 6. Comparison of T2-weighted images, lactate-to-pyruvate ratio maps, H&E staining, and hypoxia staining for a representative no therapy and combined therapy animal. A nonrigid image registration method has been used to coregister the histology to the magnetic resonance imaging (MRI) data. Magnified regions for hematoxylin and eosin (H&E) and hypoxia staining are presented next to the histology for the entire brain. Hypoxia staining (pimonidazole) shows green contrast with blue nucleus counter staining.

interest recently, but therapeutic effects on tumor metabolism are not fully understood (37). The ability to measure metabolic changes in tumors will aid to not only further understand tumor metabolism but also may also provide biomarkers to determine which therapeutic methods will be effective against tumors.

The C6 rodent glioma model was chosen to study the therapeutic response of solid tumors because this model is well established in the literature and its tumor characteristics are well defined (38, 39). During glioma progression, the tumor evolves into 2 different regions. The outer layer of tumor is highly vascularized and well-perfused, whereas the inner core of the tumor becomes necrotic and hypoxic owing to the lack of functioning or effective vasculature (40). In addition, as the tumor grows, the blood-brain barrier becomes disrupted, which can allow for increased fluid exchange with the vasculature (41). In MRI, tumors, edema, and cerebrospinal fluid appear hyperintense on T2-weighted ¹H images (42), complicating tumor volume measurements. Therefore, T1-weighted post-Gd ¹H images were used to measure tumor volumes. Given that malignant glioma possesses disrupted and leaky vasculature, low-molecular-weight paramagnetic contrast agents can effectively accumulate within the tumor (43). Post-Gd-contrast T1-weighted ¹H images were used to determine tumor volumes in this study. Contrast-enhanced tumors have increased conspicuity with hyperintense contrast compared to surrounding brain tissue for T1-weighted ¹H images. In addition, regions of edema and necrosis can be discriminated by lack of enhancement (44).

The RANO criteria are the conventional indicators of therapeutic response by monitoring tumor volume. Post-therapy success is associated with stability or recession of tumor size. Day 7 was the earliest time point when the tumor was visible in size using ¹H MRI. Then treatment was given 3 days after such animal was fully recovered from previous experiment. C6 glioma cells are known to be extremely aggressive and grow exponentially as shown Figure 3, A and C. To accommodate tumor growth and detect post-therapeutic changes, tumor volume was monitored

repeatedly every 3 days after therapy. Using the standard clinical method of detection with ¹H imaging, the earliest post-therapeutic tumor volume changes were observable only on day 18 (8 days after the therapy was given) and even later confirmed to be stable disease. Tumor recurrence was not observable in this study owing to the finite length of the study. Prolonged monitoring of post-therapeutic tumor volume changes would be required to dismiss any tumor recurrence. Considering that most malignant gliomas eventually recur despite rigorous therapies (1), early detection of therapeutic response or progression would be essential for not only prediction of prognosis but also improvement of quality of life for patients by terminating treatment when it is not effective.

Tumor metabolism is a new rising hallmark of cancer for detecting therapeutic response in early stage. For instance, metabolic changes such as upregulated glucose uptake in tumors are clinically assessed by ¹⁸F-FDG PET. However, ¹⁸F-FDG is also readily taken up by highly metabolic tissue. This leads to the possibility of false-positive results for ¹⁸F-FDG PET, which may require confirmation by other means (13, 23, 24). For example, high metabolic activity in the brain cortex can produce an elevated background signal, which confounds the interpretation of ¹⁸F-FDG PET results (25). As an alternative, radiolabeled amino acids can be used to target brain tumors because amino acids are essential to highly proliferating tissues (25, 45).

Hyperpolarized ¹³C-labeled glucose can be used in a similar manner as ¹⁸F-FDG for tumor detection and characterization; however, significant challenges exist. First, the T1 of hyperpolarized ¹³C labeled glucose is too short (<2 seconds) for detection of metabolic by-products (46). The T1 of glucose can be substantially increased by replacing all protons in the glucose with deuterium, but this significantly increases the cost of this substrate (47). Second, the labeling of various carbon atoms in the glucose molecule results in different chemical shifts for its ¹³C nuclei and those of its metabolic by-products. Often these chemical shifts are close to each other, which complicates the quantification of

metabolites as the spectrum becomes congested. In this study, we used $[1-^{13}\text{C}]$ pyruvate as the metabolic probe agent, which offers several advantages over glucose. The T_1 of $[1-^{13}\text{C}]$ pyruvate at 3 T is ~ 65 seconds in vitro (~ 45 seconds in vivo), which is long enough for pyruvate to circulate through the circulatory system of our animal model and be converted to downstream metabolites (15). Furthermore, the ^{13}C -labeled carbon can be transferred to only four different metabolites, namely, lactate, pyruvate hydrate, alanine, and bicarbonate. All these metabolites are individually represented as single spectral peaks and are well separated by their chemical shifts, producing a fully resolved spectrum, which can be readily quantified as shown in Figure 1.

Among the metabolites produced from $[1-^{13}\text{C}]$ pyruvate, the $[1-^{13}\text{C}]$ lactate signal is a sensitive biomarker for therapeutic effect in tumors where its production from pyruvate can be correlated with LDH activity and lactate pool (cellular redox state). This correlation has been previously reported in the literature (20, 29, 48, 49) where change in LDH activity can be indirectly evaluated by $[1-^{13}\text{C}]$ lactate signal. The $[1-^{13}\text{C}]$ lactate signal is normalized to the $[1-^{13}\text{C}]$ pyruvate signal to mitigate differences in pyruvate delivery and uptake in tumors compared with that of healthy brain tissue. Other preclinical studies using hyperpolarized $[1-^{13}\text{C}]$ pyruvate have observed elevated $[1-^{13}\text{C}]$ lactate signal in healthy brain tissue (50). Increased LDH activity in metabolically active tumor cells will result in an increase in the observed Lac/Pyr ratio as shown in the representative case for a rodent that received no therapy in Figure 3B. Conversely, necrotic tumor regions or healthy cells will have little to no lactate production as a result of limited LDH activity and reduced a lactate pool. Moreover, a high Lac/Pyr ratio driven by increased LDH activity in tumor can amplify the rapid progression of the tumor. This is further shown in the correlation plots of Figure 7. Here, tumor volume does not statistically correlate with the Lac/Pyr ratio. Yet, there was a moderate and statistically significant correlation between the Lac/Pyr ratio and tumor growth rate. Thus, the Lac/Pyr ratio is potentially related to the growth of tumor that indirectly coincides with increased LDH activity rather than tumor volume. This might suggest that it is possible that a measurement of the Lac/Pyr ratio at a single time point can be predictive of tumor response, at least over a short interval of time, which would otherwise require longitudinal tumor volume measurements over an extended time using conventional assessment.

As tumors rapidly grow, ineffective vascularization and necrosis of the core become evident (51). In Figure 3A, particularly on day 21, there was inadequate delivery of hyperpolarized $[1-^{13}\text{C}]$ pyruvate to regions of the tumor precluding sufficient metabolite signal for accurate quantification of the Lac/Pyr ratio. The difference in blood flow and volume between tumor and contralateral brain may indicate decreased tumor perfusion and possibly necrosis at that time point.

Conversely, as illustrated in the representative case for the rodent that received combined therapy (Figure 4B), 2 days after starting the combined therapies, the tumor already exhibited a reduced Lac/Pyr ratio compared with day 7. This ratio was comparable to that of the remaining brain tissue over the rest of the longitudinal experiment. Changes in the Lac/Pyr ratio in tumor tissue indirectly suggests a reduction in LDH activity and

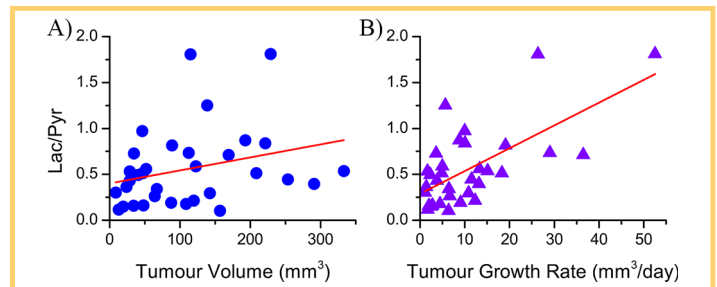


Figure 7. Correlation plots for all experimental animal groups. Correlation plot of lactate-to-pyruvate ratio in tumor versus tumor volume (A). Correlation plot of lactate-to-pyruvate ratio in tumor versus tumor growth rate (B). The Pearson correlation coefficients are 0.287 ($P = .105$) and 0.66 ($P < .001$) and R^2 values are 0.083 and 0.416 for panels (A) and (B), respectively. Tumor volumes (in mm^3) were estimated at each imaging time point from T1-weighted images acquired after contrast enhancement. An exponential growth model was fit to the tumor volume data to estimate tumor growth rate in mm^3/day .

potentially an effective therapeutic response. Measured Lac/Pyr ratios in contralateral brain declined and remained low after the window of therapy. This might be a result of reduced inflammation, which subsided after treatment caused by radiotherapy, intracranial hypertension from the growing tumor, and/or a side effect of the administration of chemotherapy (52). For this representative animal, blood flow and blood volume in the tumor and contralateral brain were also measured. The blood flow and blood volume in tumor were returned to a level consistent with the contralateral brain region ~ 14 days after therapy (data not shown). The restoration of blood flow and blood volume suggests changes in tumor vasculature owing to therapy. However, this observation can be made at only the later time points of the experiment. The large variation in blood flow and blood volume is a result of differences between the boundary of the tumor compared with the core of tumor (53). The boundary of the tumor shows increased blood flow and blood volume compared with the core when it is treated. This leads to a reduction in therapeutic efficacy near the tumor core where there is limited blood flow and blood volume.

In the clinic, patients diagnosed with glioma undergo surgery followed by radio- and chemotherapy (54). Unfortunately, the effectiveness of a particular therapeutic method for an individual patient may be unclear because of variation in tumor progression among patients. Determining the efficacy of therapy as early as possible would provide an important tool for evaluation of new therapies and improved survival for patients. As Figure 5 shows, the no therapy group shows elevated Lac/Pyr ratio sustained throughout the study, which is possibly due to increased LDH activity within the tumor. Blood flow and blood volume ratios suggests that the tumor was poorly vascularized and

necrotic; however, these data were not collected for all animals and, as a result, no absolute conclusion can be drawn

Among the 3 therapy groups (radiotherapy, chemotherapy, and combined therapy), the combined therapy group had the highest rate of survival and displayed significant reduction in the Lac/Pyr ratio within the tumors. Combined therapy is expected to induce greater DNA damage compared with a single therapy alone, which leads to cellular apoptosis, lactate production, and tumor burden (55). In the literature, significant evidence exists suggesting radiotherapy helps to increase vasculature permeability and improve delivery of chemotherapeutic drugs to tumor sites (56, 57). The chemotherapy group showed a statistically significant reduction of the Lac/Pyr ratio in tumors; however, this group of rats had a high rate of mortality. Chemotherapy animals lost a significant amount of weight after therapy despite a moderate dose of temozolomide given to those rats (58, 59). Temozolomide is known to cause nausea, vomiting, fatigue, and headache as adverse reactions in human (59, 60). These side effects, may have been the cause of weight loss for these animals, which negatively impacted their survivability. This may suggest that chemotherapy on its own is sufficient to cause dysfunction in tumor metabolism and proliferation; however, it is not potent enough alone to extend survival. Furthermore, dimethyl sulfoxide was used as a vehicle for delivering temozolomide. The repeated dose used for injection (~3.6 g/kg) was far less than the tolerance dose (8.2 g/kg) (61). The radiotherapy group had a slow and a nonstatistically significant decline in the Lac/Pyr ratio, yet this group had low mortality compared with the chemotherapy group. In fact, there was a large variation in the Lac/Pyr ratio after therapy among the radiotherapy group, suggesting that the radiotherapy efficacy varies among the cohort. Despite injecting approximately the same number of C6 cells and providing a standard conformal radiation dose, an individual animal can show a varied therapeutic response to radiotherapy. Those tumors that did not respond to radiotherapy may indicate resistance to therapy and tumor recurrence. However, an expanded study in the future with extended timeline would be required to establish the metabolic profile associated with resistance to therapy and potential recurrence. This longer longitudinal imaging study may also be able to assess the prognostic ability of the Lac/Pyr ratio to predict therapeutic outcomes. To be definitive, this will require a carefully constructed set of experimental protocols.

Lastly, Figure 6 presents histological validation of Lac/Pyr measurements in the tumor model. Histological sections have been coregistered to the MRI data for accurate comparison.

ACKNOWLEDGMENTS

We thank the laboratories of Dr. Paula Foster (specifically Drs. Yuanxin Chen and Amanda Hamilton) and Dr. Steven Kerfoot (Dr. Heather Craig), as well as Jennifer

Tumor location and size are apparent from H&E images and with ¹H MRI. Although the T2-weighted contrast would suggest that the tumors are relatively homogenous, at least in structure, it is apparent from the Lac/Pyr ratio map and hypoxia staining that tumor metabolism varies throughout the tumor. The untreated tumor shows strong hypoxia staining and a high Lac/Pyr ratio. As previously noted in the literature, tumor hypoxia can enhance LDH expression and thus increase lactate production. However, following effective therapy, the large reduction in the Lac/Pyr ratio shown in the combined therapy group compared with the no therapy group suggests a reduction in LDH activity via decrease in lactate production. This is further verified by differences in hypoxia staining between these 2 cohorts. For the untreated tumor, increased lactate production associated with a hypoxic tumor environment with insufficient or inefficient vascularization was verified by hypoxia staining at endpoint. For the combined therapy group, reduced hypoxia was observed commensurate with the lower measured Lac/Pyr ratios. Looking forward to clinical translation, these findings suggest that the Lac/Pyr ratio is a noninvasive imaging biomarker for assessment of hypoxia in the tumor microenvironment, which may be a useful tool for early assessment of tumor response to therapy.

In summary, this study examined longitudinal therapeutic response to different therapies using hyperpolarized [1-¹³C]pyruvate MRSI. For cases where a standard treatment is ineffective, early assessment of therapeutic response is highly desirable to prompt alternative or salvage therapies or to improve end-of-life care. We have observed different early therapeutic responses assessed by changes in the Lac/Pyr ratio of tumor. All therapies produced unique changes in the Lac/Pyr ratio compared with the no therapy control group. In contrast, therapeutic assessment using tumor volume showed a time-course like that assessed by the Lac/Pyr ratio; yet, significant changes were not discernable until much later after therapy. Heterogeneous response to therapies observed in individual animals and across therapy groups was well characterized by hyperpolarized [1-¹³C]pyruvate MRSI. The Lac/Pyr ratio measured across therapy groups was shown to be correlated with tumor growth after initiation of therapy. Regional differences in the Lac/Pyr ratio were compared with histology at endpoint and have been shown to be consistent with hypoxia. In conclusion, this study shows the use of hyperpolarized [1-¹³C]pyruvate to probe real-time tumor metabolism, which can provide a useful longitudinal noninvasive biomarker for assessment of therapeutic response.

Hadway, for initial help with our tumor model. We also gratefully recognize funding from the Cancer Imaging Network of Ontario and the Ontario Institute for Cancer Research.

REFERENCES

1. Wen PY, Kesari S. Malignant gliomas in adults. *N Engl J Med*. 2008;359:492–507.
2. Ostrom QT, Gittleman H, Fulop J, Liu M, Blanda R, Kromer C, Wolinsky Y, Kruchko C, Barnholtz-Sloan JS. CBTRUS Statistical Report: primary Brain and Central Nervous System Tumors Diagnosed in the United States in 2008–2012. *Neuro Oncol*. 2015;17 :iv1–iv62.
3. Li J, Di C, Mattox AK, Wu L, Adamson DC. The future role of personalized medicine in the treatment of glioblastoma multiforme. *Pharmgenomics Pers Med*. 2010;3:111–127.
4. Bradley WG, Jr., Waluch V, Yadley RA, Wycoff RR. Comparison of CT and MR in 400 patients with suspected disease of the brain and cervical spinal cord. *Radiology*. 1984;152:695–702.

5. Mehta AI, Kanaly CW, Friedman AH, Bigner DD, Sampson JH. Monitoring radiographic brain tumor progression. *Toxins*. 2011;3:191–200.
6. Wen PY, Macdonald DR, Reardon DA, Cloughesy TF, Sorensen AG, Galanis E, DeGroot J, Wick W, Gilbert MR, Lassman AB, Tsien C, Mikkelsen T, Wong ET, Chamberlain MC, Stupp R, Lamborn KR, Vogelbaum MA, van den Bent MJ, Chang SM. Updated response assessment criteria for high-grade gliomas: response assessment in neuro-oncology working group. *J Clin Oncol*. 2010;28:1963–1972.
7. Hanahan D, Weinberg RA. Hallmarks of Cancer: the Next Generation. *Cell*. 2011;144:646–674.
8. Kroemer G, Pouyssegur J. Tumor cell metabolism: cancer's Achilles' heel. *Cancer Cell*. 2008;13:472–482.
9. Brahim-Horn MC, Chiche J, Pouyssegur J. Hypoxia signalling controls metabolic demand. *Curr Opin Cell Biol*. 2007;19:223–229.
10. Gatenby RA, Gillies RJ. Why do cancers have high aerobic glycolysis? *Nat Rev Cancer*. 2004;4:891–899.
11. Kennedy KM, Dewhirst MW. Tumor metabolism of lactate: the influence and therapeutic potential for MCT and CD147 regulation. *Future Oncol*. 2010;6:127–148.
12. Mankoff DA, Eary JF, Link JM, Muzi M, Rajendran JG, Spence AM, Krohn KA. Tumor-specific positron emission tomography imaging in patients: [18F] fluorodeoxyglucose and beyond. *Clin Cancer Res*. 2007;13:3460–3469.
13. Weber WA, Avril N, Schwaiger M. Relevance of positron emission tomography (PET) in oncology. *Strahlenther Onkol*. 1999;175:356–373.
14. Ardenkjaer-Larsen JH, Fridlund B, Gram A, Hansson G, Hansson L, Lerche MH, Servin R, Thaning M, Golman K. Increase in signal-to-noise ratio of >10,000 times in liquid-state NMR. *Proc Natl Acad Sci U S A*. 2003;100:10158–10163.
15. Chattergoon N, Martinez-Santesteban F, Handler WB, Ardenkjaer-Larsen JH, Scholl TJ. Field dependence of T1 for hyperpolarized [1-¹³C]pyruvate. *Contrast Media Mol Imaging*. 2013;8:57–62.
16. Gallagher FA, Kettunen MI, Brindle KM. Biomedical applications of hyperpolarized C-13 magnetic resonance imaging. *Prog Nucl Mag Res Sp*. 2009;55:285–295.
17. Pinheiro C, Longatto-Filho A, Azevedo-Silva J, Casal M, Schmitt FC, Baltazar F. Role of monocarboxylate transporters in human cancers: state of the art. *J Bioenerg Biomembr*. 2012;44:127–139.
18. Phan LM, Yeung SC, Lee MH. Cancer metabolic reprogramming: importance, main features, and potentials for precise targeted anti-cancer therapies. *Cancer Biol Med*. 2014;11:1–19.
19. Tennant DA, Duran RV, Gottlieb E. Targeting metabolic transformation for cancer therapy. *Nat Rev Cancer*. 2010;10:267–277.
20. Dafni H, Larson PEZ, Hu S, Yoshihara HAJ, Ward CS, Venkatesh HS, Wang C, Zhang X, Vigneron DB, Ronen SM. Hyperpolarized ¹³C spectroscopic imaging informs on hypoxia-inducible factor-1 and myc activity downstream of platelet-derived growth factor receptor. *Cancer Res*. 2010;70:7400–7410.
21. Witney TH, Kettunen MI, Brindle KM. Kinetic modeling of hyperpolarized ¹³C label exchange between pyruvate and lactate in tumor cells. *J Biol Chem*. 2011;286:24572–24580.
22. Chaumeil MM, Ozawa T, Park I, Scott K, James CD, Nelson SJ, Ronen SM. Hyperpolarized ¹³C MR spectroscopic imaging can be used to monitor Everolimus treatment in vivo in an orthotopic rodent model of glioblastoma. *NeuroImage*. 2012;59:193–201.
23. Zhu A, Lee D, Shim H. Metabolic positron emission tomography imaging in cancer detection and therapy response. *Semin Oncol*. 2011;38:55–69.
24. Strauss LG. Fluorine-18 deoxyglucose and false-positive results: a major problem in the diagnostics of oncological patients. *Eur J Nucl Med*. 1996;23:1409–1415.
25. Ledezma CJ, Chen W, Sai V, Freitas B, Cloughesy T, Czernin J, Pope W. 18F-FDOPA PET/MRI fusion in patients with primary/recurrent gliomas: initial experience. *Eur J Radiol*. 2009;71:242–248.
26. Lin RY, Vera JC, Chaganti RS, Golde DW. Human monocarboxylate transporter 2 (MCT2) is a high affinity pyruvate transporter. *J Biol Chem*. 1998;273:28959–28965.
27. Park JM, Josan S, Jang T, Merchant M, Yen Y-F, Hurd RE, Recht L, Spielman DM, Mayer D. Metabolite kinetics in C6 rat glioma model using magnetic resonance spectroscopic imaging of hyperpolarized [1-¹³C]pyruvate. *Magn Reson Med*. 2012;68:1886–1893.
28. Day SE, Kettunen MI, Cherukuri MK, Mitchell JB, Lizak MJ, Morris HD, Matsumoto S, Koretsky AP, Brindle KM. Detecting response of rat C6 glioma tumors to radiotherapy using hyperpolarized [1-¹³C]pyruvate and ¹³C magnetic resonance spectroscopic imaging. *Magn Reson Med*. 2011;65:557–563.
29. Day SE, Kettunen MI, Gallagher FA, Hu D-E, Lerche M, Wolber J, Golman K, Ardenkjaer-Larsen JH, Brindle KM. Detecting tumor response to treatment using hyperpolarized C-13 magnetic resonance imaging and spectroscopy. *Nat Med*. 2007;13:1382–1387.
30. Park I, Bok R, Ozawa T, Phillips JJ, James CD, Vigneron DB, Ronen SM, Nelson SJ. Detection of early response to temozolomide treatment in brain tumors using hyperpolarized C-13 MR metabolic imaging. *J Magn Reson Imaging*. 2011;33:1284–1290.
31. Friesen-Waldner L, Chen A, Mander W, Scholl TJ, McKenzie CA. Optimisation of dynamic nuclear polarisation of [1-¹³C] pyruvate by addition of gadolinium-based contrast agents. *J Magn Reson*. 2012;223:85–89.
32. Lim H, Thind K, Martinez-Santesteban FM, Scholl TJ. Construction and evaluation of a switch-tuned (13) C - (1) H birdcage radiofrequency coil for imaging the metabolism of hyperpolarized (13) C-enriched compounds. *J Magn Reson Imaging*. 2014;40:1082–1090.
33. Jensen MD, Hrinivich WT, Jung JA, Holdsworth DW, Drangova M, Chen J, Wong E. Implementation and commissioning of an integrated micro-CTRT system with computerized independent jaw collimation. *Med Phys*. 2013;40:081706.
34. Gibson E, Cruckley C, Gaed M, Gómez JA, Moussa M, Chin JL, Bauman GS, Fenster A, Ward AD. Registration of prostate histology images to ex vivo MR images via strand-shaped fiducials. *J Magn Reson Imaging*. 2012;36:1402–1412.
35. Keeler J. Understanding NMR spectroscopy. 2nd ed. Chichester, U.K.: John Wiley and Sons; 2010. xiii, 511.
36. Yushkevich PA, Piven J, Hazlett HC, Smith RG, Ho S, Gee JC, Gerig G. User-guided 3D active contour segmentation of anatomical structures: significantly improved efficiency and reliability. *NeuroImage*. 2006;31:1116–1128.
37. Vander Heiden MG. Targeting cancer metabolism: a therapeutic window opens. *Nat Rev Drug Discov*. 2011;10:671–684.
38. Grobben B, De Deyn PP, Slegers H. Rat C6 glioma as experimental model system for the study of glioblastoma growth and invasion. *Cell Tissue Res*. 2002;310:257–270.
39. Barth RF, Kaur B. Rat brain tumor models in experimental neuro-oncology: the C6, 9L, T9, RG2, F98, BT4C, RT-2 and CNS-1 gliomas. *J Neurooncol*. 2009;94:299–312.
40. Vajkoczy P, Schilling L, Ullrich A, Schmiedek P, Menger MD. Characterization of angiogenesis and microcirculation of high-grade glioma: an intravital multicolor fluorescence microscopic approach in the athymic nude mouse. *J Cereb Blood Flow Metab*. 1998;18:510–520.
41. Erdlenbruch B, Alipour M, Fricker G, Miller DS, Kugler W, Eibl H, Lakomek M. Alkylglycerol opening of the blood-brain barrier to small and large fluorescence markers in normal and C6 glioma-bearing rats and isolated rat brain capillaries. *Br J Pharmacol*. 2003;140:1201–1210.
42. Drevelgas A. Imaging of brain tumors with histological correlations. 2nd ed. Berlin: Springer; 2011. x, 432.
43. Graif M, Bydder GM, Steiner RE, Niendorf P, Thomas DJG, Young IR. Contrast-enhanced MR imaging of malignant brain tumors. *AJNR Am J Neuroradiol*. 1985;6:855–862.
44. Steen RG. Edema and tumor perfusion: characterization by quantitative 1H MR imaging. *AJR Am J Roentgenol*. 1992;158:259–264.
45. Becherer A, Karanikas G, Szab M, Zettinig G, Asenbaum S, Marosi C, Henk C, Wunderbaldinger P, Czech T, Wadsak W, Kletter K. Brain tumour imaging with PET: a comparison between [18F]fluorodopa and [11C]methionine. *Eur J Nucl Med Mol Imaging*. 2003;30:1561–1567.
46. Harada M, Kubo H, Abe T, Maezawa H, Otsuka H. Selection of endogenous ¹³C substrates for observation of intracellular metabolism using the dynamic nuclear polarization technique. *Jpn J Radiol*. 2010;28:173–179.
47. Allouche-Arnon H, Wade T, Waldner LF, Miller VN, Gomori JM, Katz-Brull R, McKenzie CA. In vivo magnetic resonance imaging of glucose - initial experience. *Contrast Media Mol Imaging*. 2013;8:72–82.
48. Chen AP, Chu W, Gu Y-P, Cunningham CH. Probing early tumor response to radiation therapy using hyperpolarized [1-(13)C]pyruvate in MDA-MB-231 xenografts. *PLoS One*. 2013;8:e56551.
49. Albers MJ, Bok R, Chen AP, Cunningham CH, Zierhut ML, Zhang YV, Kohler SJ, Tropp J, Hurd RE, Yen Y-F, Nelson SJ, Vigneron DB, Kurhanewicz J. Hyperpolarized ¹³C lactate, pyruvate, and alanine: noninvasive biomarkers for prostate cancer detection and grading. *Cancer Res*. 2008;68:8607–8615.
50. Miloshev VZ, Granlund KL, Bolyanskiy R, Lyashchenko SK, DeAngelis LM, Mellingshoff IK, Brennan CW, Tabar V, Yang TJ, Holodny AI, Sosa RE, Guo YW, Chen AP, Tropp J, Robb F, Keshari KR. Metabolic imaging of the human brain with hyperpolarized (13)C pyruvate demonstrates (13)C lactate production in brain tumor patients. *Cancer Res*. 2018;78:3755–3760.
51. Raza SM, Lang FF, Aggarwal BB, Fuller GN, Wildrick DM, Sawaya R. Necrosis and glioblastoma: a friend or a foe? A review and a hypothesis. *Neurosurgery*. 2002;51:2–12; discussion 3.
52. Thind K, Jensen MD, Hegarty E, Chen AP, Lim H, Martinez-Santesteban F, Van Dyk J, Wong E, Scholl TJ, Santyr GE. Mapping metabolic changes associated with early radiation induced lung injury post conformal radiotherapy using hyperpolarized (1) (3)C-pyruvate magnetic resonance spectroscopic imaging. *Radiother Oncol*. 2014;110:317–322.
53. Ulmer S, Liess C, Kesari S, Otto N, Straube T, Jansen O. Use of dynamic susceptibility-contrast MRI (DSC-MRI) to assess perfusion changes in the ipsilateral brain parenchyma from glioblastoma. *J Neurooncol*. 2009;91:213–220.
54. Norden AD, Wen PY. Glioma therapy in adults. *Neurologist*. 2006;12:279–292.
55. Frosina G. DNA repair and resistance of gliomas to chemotherapy and radiotherapy. *Mol Cancer Res*. 2009;7:989–999.

56. Lammers T, Peschke P, Kühnlein R, Subr V, Ulbrich K, Debus J, Huber P, Hennink W, Storm G. Effect of radiotherapy and hyperthermia on the tumor accumulation of HPMA copolymer-based drug delivery systems. *J Control Release*. 2007;117:333–341.
57. Jain RK. Normalization of tumor vasculature: an emerging concept in antiangiogenic therapy. *Science*. 2005;307:58–62.
58. Stepanenko AA, Andreieva SV, Korets KV, Mykytenko DO, Baklaushev VP, Huleyuk NL, Kovalova OA, Kotsarenko KV, Chekhonin VP, Vassetzky YS, Avdieiev SS, Dmitrenko VV. Temozolomide promotes genomic and phenotypic changes in glioblastoma cells. *Cancer Cell Int*. 2016;16:36.
59. Zhang YH, Zhang H, Liu JM, Yue ZJ. Temozolomide/PLGA microparticles: a new protocol for treatment of glioma in rats. *Med Oncol*. 2011;28:901–906.
60. Stupp R, Mason WP, van den Bent MJ, Weller M, Fisher B, Taphoorn MJB, Belanger K, Brandes AA, Marosi C, Bogdahn U, Curschmann J, Janzer RC, Ludwin SK, Gorlia T, Allgeier A, Lacombe D, Cairncross JG, Eisenhauer E, Mirimanoff RO. Radiotherapy plus concomitant and adjuvant temozolomide for glioblastoma. *N Engl J Med*. 2005;352:987–996.
61. Smith ER, Hadidian Z, Mason MM. The single- and repeated-dose toxicity of dimethyl sulfoxide. *Ann NY Acad Sci*. 1967;141:96–109.